

Article

Nonlinear Isotherm and Kinetic Modeling of Cu(II) and Pb(II) Uptake from Water by MnFe₂O₄/Chitosan Nanoadsorbents

Manny Anthony M. Taguba^{1,2}, Dennis C. Ong³ , Benny Marie B. Ensano⁴ , Chi-Chuan Kan⁵ ,
Nurak Grisdanurak⁶, Jurng-Jae Yee^{7,*} and Mark Daniel G. de Luna^{2,8,*} 

¹ College of Engineering, National University, Manila 1008, Philippines; mmtaguba@national-u.edu.ph

² Environmental Engineering Program, National Graduate School of Engineering, University of the Philippines Diliman, Quezon City 1101, Philippines

³ School of Technology, University of the Philippines Visayas, Miagao, Iloilo 5023, Philippines; dcong@up.edu.ph

⁴ University Core Research Center for Disaster-Free and Safe Ocean City Construction, Dong-A University, Busan 49315, Korea; bmensano@dau.ac.kr

⁵ Institute of Hot Spring Industry, Chia-Nan University of Pharmacy and Science, Tainan 71710, Taiwan; cckanev@mail.cnu.edu.tw

⁶ Center of Excellence in Environmental Catalysis and Adsorption, Faculty of Engineering, Thammasat University, Pathumthani 12120, Thailand; gnurak@engr.tu.ac.th

⁷ Department of Architectural Engineering, Dong-A University, Busan 49315, Korea

⁸ Department of Chemical Engineering, University of the Philippines Diliman, Quezon City 1101, Philippines

* Correspondence: jjyee@dau.ac.kr (J.-J.Y.); mgdeluna@up.edu.ph (M.D.G.d.L.)



Citation: Taguba, M.A.M.; Ong, D.C.; Ensano, B.M.B.; Kan, C.-C.; Grisdanurak, N.; Yee, J.-J.; de Luna, M.D.G. Nonlinear Isotherm and Kinetic Modeling of Cu(II) and Pb(II) Uptake from Water by MnFe₂O₄/Chitosan Nanoadsorbents. *Water* **2021**, *13*, 1662. <https://doi.org/10.3390/w13121662>

Academic Editor: Laura Bulgariu

Received: 14 May 2021

Accepted: 8 June 2021

Published: 14 June 2021

Publisher's Note: MDPI stays neutral with regard to jurisdictional claims in published maps and institutional affiliations.



Copyright: © 2021 by the authors. Licensee MDPI, Basel, Switzerland. This article is an open access article distributed under the terms and conditions of the Creative Commons Attribution (CC BY) license (<https://creativecommons.org/licenses/by/4.0/>).

Abstract: Researchers are in continuous search of better strategies to minimize, if not prevent, the anthropogenic release of toxic heavy metals, such as Cu(II) and Pb(II), into drinking water resources and the natural environment. Herein, we report for the first time the low-temperature combustion synthesis of magnetic chitosan-manganese ferrite in the absence of toxic cross-linking agents and its removal of Cu(II) and Pb(II) from single-component metal solutions. The nonlinear Langmuir model best described the isotherm data, while the nonlinear pseudo-second order model best described the kinetic data, signifying monolayer Cu(II) or Pb(II) adsorption and chemisorption as the rate-determining step, respectively. Adsorption capacities by magnetic chitosan-manganese ferrite obtained for both metals were consistently higher than those by manganese ferrite, indicating that chitosan enhanced the performance of the magnetic adsorbent. The maximum adsorption capacities of magnetic chitosan-manganese ferrite for Cu(II) and Pb(II) were 14.86 and 15.36 mg g⁻¹, while that of manganese ferrite were 2.59 and 13.52 mg g⁻¹, respectively. Moreover, the adsorbents showed superior binding affinity and sorption for Pb(II) than Cu(II) owing to the stronger ability of the former to form inner-sphere complexes with manganese ferrite and magnetic chitosan-manganese ferrite. Finally, thermodynamic studies revealed that the uptake of either Pb(II) or Cu(II) by magnetic chitosan-manganese ferrite was spontaneous and endothermic. The as-prepared adsorbent was characterized for morphology, elemental composition, surface functional sites, and particle size using scanning electron microscopy, energy dispersive spectroscopy, Fourier transform infrared spectroscopy, and dynamic light scattering technique, respectively.

Keywords: adsorption; chitosan; heavy metals; nanotechnology; water treatment

1. Introduction

Heavy metals have been beneficial in improving the quality of human life, but their excessive use and consumption have resulted in serious environmental and health problems. For instance, copper (Cu) and its compounds have been used as algacide in aquaculture [1], blue pigment in electronic inks [2], and adsorbents in carbon dioxide capture technology [3]. Meanwhile, various cellular processes utilize copper as an enzyme cofactor [4]. However, copper ions have been found to inhibit plant growth and root development

when assimilated in excess. Moreover, high copper intake in humans and animals has been linked to various forms of physiological and neurological damage [5–7]. Lead (Pb), a primary ingredient in batteries, ammunition, and paints, is another metal of concern [8,9]. Unlike copper, lead has no useful purpose and is extremely toxic to the human body. The International Agency for Research on Cancer has categorized lead-containing inorganic compounds under “Group 2A: probably carcinogenic to humans” [10]. Acute exposure to high lead concentrations can result in anorexia, irritability, poor attention span, constipation, abdominal pain, vomiting, reversible kidney damage, muscle weakness, anemia, encephalopathy, coma, and death [11,12].

In recent years, ion concentrations of copper (Cu(II)) and lead (Pb(II)) in some drinking water sources have exceeded both the local and international allowable limits. In New South Wales (Australia), 5% of Cu(II)- and 8% of Pb(II)-contaminated tap water samples had exceeded the Australian Drinking Water Guidelines, which are 2.0 and 0.010 mg L⁻¹, respectively [13]. In Kerman City (Iran), Pb(II) in groundwater reached up to 0.045 mg L⁻¹ surpassing the World Health Organization (WHO, 0.01 mg L⁻¹) and United States Environmental Protection Agency (US EPA, 0.015 mg L⁻¹) drinking water standards for Pb(II) [14]. In order to comply with the stringent regulations and ensure safe potable water for the community, many researchers worldwide continue to develop effective and economical treatment technologies for the abatement of heavy metal ions from drinking water sources.

Several physicochemical treatment methods have demonstrated adequate performance in heavy metal abatement of water matrices but remain economically non-viable because of the additional capital and operational costs. Adsorption, however, remains a feasible alternative, especially in developing countries, because it is environmentally benign, simple, inexpensive, and does not produce large sludge quantities [15]. In recent decades, various natural and synthetic adsorbents have been examined for their ability to remove heavy metals from contaminated solutions [16–19], yet separating these adsorbents from the water matrix entails a complex process and additional cost.

Recently, magnetic adsorbents have garnered interest in the scientific community because these can readily be separated from aqueous solutions [20]. In a study on Pb(II) and Cu(II) adsorption by iron(III) oxide- and iminodiacetic acid-modified peanut husks, it was found that magnetization enhanced metal removal efficiency (i.e., 0.36 mmol g⁻¹ for Pb(II) and 0.75 mmol g⁻¹ for Cu(II)) and ensured faster separation of the biosorbent from the solution [21]. In another study, magnetite-layered double hydroxide-based nanosorbent simultaneously removed 110.25 mg g⁻¹ Cu(II), 190.75 mg g⁻¹ Pb(II) and 140.50 mg g⁻¹ Cd(II) from contaminated solutions [22]. Meanwhile, spinel ferrite is a novel adsorbent material with superparamagnetic properties that is formed by combining metallic ions (i.e., Mg(II), Mn(II), Co(II), Ni(II), etc.) and ferric ions (Fe₂O₄) [23]. Of the various types, manganese ferrite (MFO, MnFe₂O₄) is considered superior in terms of specific surface area, magnetic properties, and adsorption performance [24,25]. Manganese ferrite can be used as a heavy metal adsorbent in aqueous solutions because iron and manganese-based oxides are excellent heavy metal scavengers owing to their high affinity for metal ions under natural pH conditions [15,26,27]. Moreover, the surface functionalization and coating of MFO with a protective layer can conserve its magnetic properties and improve its stability [28].

Chitosan possesses polycationic chelating properties in its surface amino and hydroxyl groups, which makes it a highly-favorable material to functionalize magnetic nanoparticles [29]. Chitosan alone is a promising heavy metal adsorbent, but its adsorptive capabilities are restricted due to its pH sensitivity and weak mechanical properties [30]. Typical preparation of magnetic chitosan nanocomposites is carried out either via a complicated multi-step synthesis method or a suspension cross-linking technique that uses harmful reagents (i.e., glutaraldehyde) [31]. Glutaraldehyde, a low-molecular-weight aldehyde, has been confirmed by *in vitro* and *in vivo* studies to cause chronic bronchitis, skin irritation, bone marrow hyperplasia, and leukemia upon prolonged inhalation or ingestion [32,33].

Therefore, the main goal of this study is to integrate the excellent adsorptive properties of manganese ferrite and those of chitosan into one material via a simple low-temperature combustion technique without using toxic cross-linking agents. The as-prepared adsorbent was characterized for morphology, elemental composition, surface functional sites, and particle size using scanning electron microscopy (SEM), energy dispersive spectroscopy (EDS), Fourier transform infra-red (FTIR) spectroscopy, and dynamic light scattering (DLS) technique, respectively. The adsorptive behavior of MFO and the magnetic chitosan-manganese ferrite (CMFO) on the uptake of Cu(II) or Pb(II) ions was assessed and compared through kinetic, isotherm, and thermodynamic studies, using nonlinear modeling whenever possible. The influence of the presence of competing ion on the adsorption capacity of MFO and CMFO was also investigated.

2. Materials and Methods

2.1. Chemicals and Reagents

Analytical grade reagents were used as received. Manganese(II) nitrate tetrahydrate ($\text{Mn}(\text{NO}_3)_2 \cdot 4\text{H}_2\text{O}$), iron(III) nitrate nonahydrate ($\text{Fe}(\text{NO}_3)_3 \cdot 9\text{H}_2\text{O}$), urea (NH_2CONH_2), and sodium nitrate (NaNO_3) were procured from Panreac AppliChem (Spain). Chitosan [$(\text{C}_6\text{H}_{11}\text{NO}_4)_n$], with a 96% degree of deacetylation and 200 kDa average molecular weight, was purchased from Acros Organics (Taiwan). Copper(II) nitrate trihydrate ($\text{Cu}(\text{NO}_3)_2 \cdot 3\text{H}_2\text{O}$) and lead(II) nitrate ($\text{Pb}(\text{NO}_3)_2$) were both obtained from Ferak Berlin (Germany). Sodium hydroxide pellets (NaOH , 99.38%) and hydrochloric acid (HCl , 37%), used for pH adjustment, were acquired from Choneye Pure Chemical (Taiwan) and Merck (Germany), respectively. ICP multi-element standard solution was obtained from Merck (Germany) while deionized (DI) water (18.2 M Ω -cm), used in preparing solutions, was collected using Purelab Ultra by ELGA LabWater (UK).

2.2. Adsorbent Preparation

MFO was synthesized using the modified low-temperature combustion technique of Sam and Nesaraj [34]. A 1:2 molar proportion of $\text{Mn}(\text{NO}_3)_2 \cdot 4\text{H}_2\text{O}$ and $\text{Fe}(\text{NO}_3)_3 \cdot 9\text{H}_2\text{O}$ was dissolved in 50 mL of deionized water and continuously stirred for 2 h at 50 rpm and 40 °C. Then, 10 g of urea was added and the resulting solution was combusted in a flap door muffle furnace (Nabertherm, P330, Germany) at 550 °C for 130 min. When the reactions were completed, the resulting crispy dark particles were ground using a mortar and pestle. The pulverized ferrites were separated using a hand magnet, washed several times with DI water, and finally dried at 100 °C for 12 h in a Memmert UFE 400 laboratory oven (Germany).

In the preparation of CMFO, about 1 g of chitosan was added dropwise to 50 mL of 0.5 M HCl under vigorous stirring for 2 h. Next, 5 g of MFO was added to the chitosan solution and the solution pH was adjusted to neutral pH (~7.0) using 0.2 M NaOH. The resulting mixture was sieved using mesh #200 (0.074 mm mesh diameter) and washed repeatedly with deionized water. After this, the magnetic particles were separated by a hand magnet and placed in an oven at 90 °C for 24 h. The oven-dried solid was then pulverized using a mortar and pestle.

2.3. Instrumentation and Analytical Methods

The surface functional groups of the as-prepared magnetic sorbents were recorded using a Jasco FT/IR-410 Fourier transform infrared spectrometer (FTIR). Before the FTIR analysis, the samples were mixed with potassium bromide (KBr, Merck, Germany) at a 1:20 weight ratio and pressed into a translucent disk (7 mm die set, Pike Technologies) under vacuum. The average particle size of the as-prepared adsorbents was determined using dynamic light scattering. The morphology of the synthesized adsorbents was assessed by employing a field-emission scanning electron microscope with energy dispersive spectroscopy (FE-SEM/EDS), wherein a dual beam Helios Nano lab 600i was used at an accelerating voltage of 15.0 kV. The amount of adsorbed metal ion was quantified using

an inductively-coupled plasma-optical emission spectrometer (ICP-OES, Optima 2000 DV Perkin Elmer, Australia). Standard ICP multi-metal solution for the instrument's calibration curve was prepared at different concentrations (0.1, 0.3, 0.5, 1, 3, 7, and 10 mg L⁻¹).

2.4. Adsorption Studies

Batch adsorption experiments were carried out in a 100 mL Erlenmeyer flask containing 25 mL of 200 mg L⁻¹ single-component metal solution (Cu(NO₃)₂·3H₂O or Pb(NO₃)₂). The solution pH was adjusted to 4.5 using 0.1 M NaOH and 0.1 M HCl solutions to simulate the typical pH of wastewaters (pH 4–6). About 0.1 g of the adsorbent (CMFO or MFO) was then added, and the mixture was agitated in a reciprocal shaker bath (Yih Der BT-350, Taiwan) at 100 rpm and 25 °C for 24 h. Afterwards, the mixture was filtered with Whatman 40 ashless filter paper (GE Healthcare, UK) having a nominal particle retention of 8 µm. The obtained filtrate was further filtered using a nylon syringe filter (0.45 µm pore size) to eliminate particle intrusion into the analytical equipment. Lastly, the residual metal concentration was quantified using ICP-OES. The adsorption capacity (q_e , mg g⁻¹) or the amount of heavy metal ion adsorbed onto CMFO and MFO was computed following Equation (1):

$$q_e = \frac{(C_0 - C_e)}{m} V \quad (1)$$

where C_0 is the initial metal ion concentration (mg L⁻¹), C_e is the equilibrium metal ion concentration (mg L⁻¹), V is the solution volume (L), and m is the adsorbent mass (g).

Isotherm, kinetic, and thermodynamic studies were conducted using the same experimental procedure and conditions as above, except that for isotherm study, initial metal concentration was varied from 25 to 200 mg L⁻¹, for kinetic study, the contact time ranged between 1 and 36 h, and for thermodynamic studies, varying temperatures (i.e., 25, 35, and 45 °C) were used. The effect of ionic strength on the Cu(II) or Pb(II) uptake by CMFO and MFO was also investigated by adding varying amounts of NaNO₃ (0.02 to 2.12 mol L⁻¹) to 25 mg L⁻¹ of heavy metal solution at pH 4.50, 100 rpm and 25 °C for 24 h.

3. Results and Discussion

3.1. Adsorbent Characterization

Scanning electron microscopy (SEM) was used to examine the morphologies of the synthesized CMFO and MFO adsorbents. The SEM images of MFO in Figure 1a,b, taken at 100× and 10,000× magnifications, respectively, displayed a rough surface with deep cracks. CMFO (Figure 1c,d), on the other hand, showed agglomerated particles on a much rougher surface, attributed to chitosan. Clearly, the coating with chitosan resulted in a heterogenic surface structure of the adsorbent, which contributed to the enhancement of the adsorption sites. The qualitative EDS spectra for MFO (Figure 1e) confirmed the major presence of Fe, Mn, and O, which was consistent with a previous study [24]. The C and N peaks between 0.2–0.5 keV in Figure 1e are attributed to the entrapped residual urea in MFO, with N peak likely obscured by the broad O peak in this region. Meanwhile, the EDS spectra for CMFO (Figure 1f) showed a higher intensity peak of C and small N peak, in addition to Fe, Mn, and O, which are ascribed to the chitosan coating [35]. Again, the N peak may be hidden and/or combined with the O peak in the region of 0.4–0.5 keV [36].

Particle sizes of synthesized magnetic adsorbents were measured using dynamic light scattering. Chitosan-manganese ferrite composite (average particle size = 203 nm) had relatively-larger sizes than MFO (average particle size = 172 nm), which confirms that the magnetic composite was successfully coated with chitosan. Moreover, the prepared MFO in this study is comparable with previous findings [34].

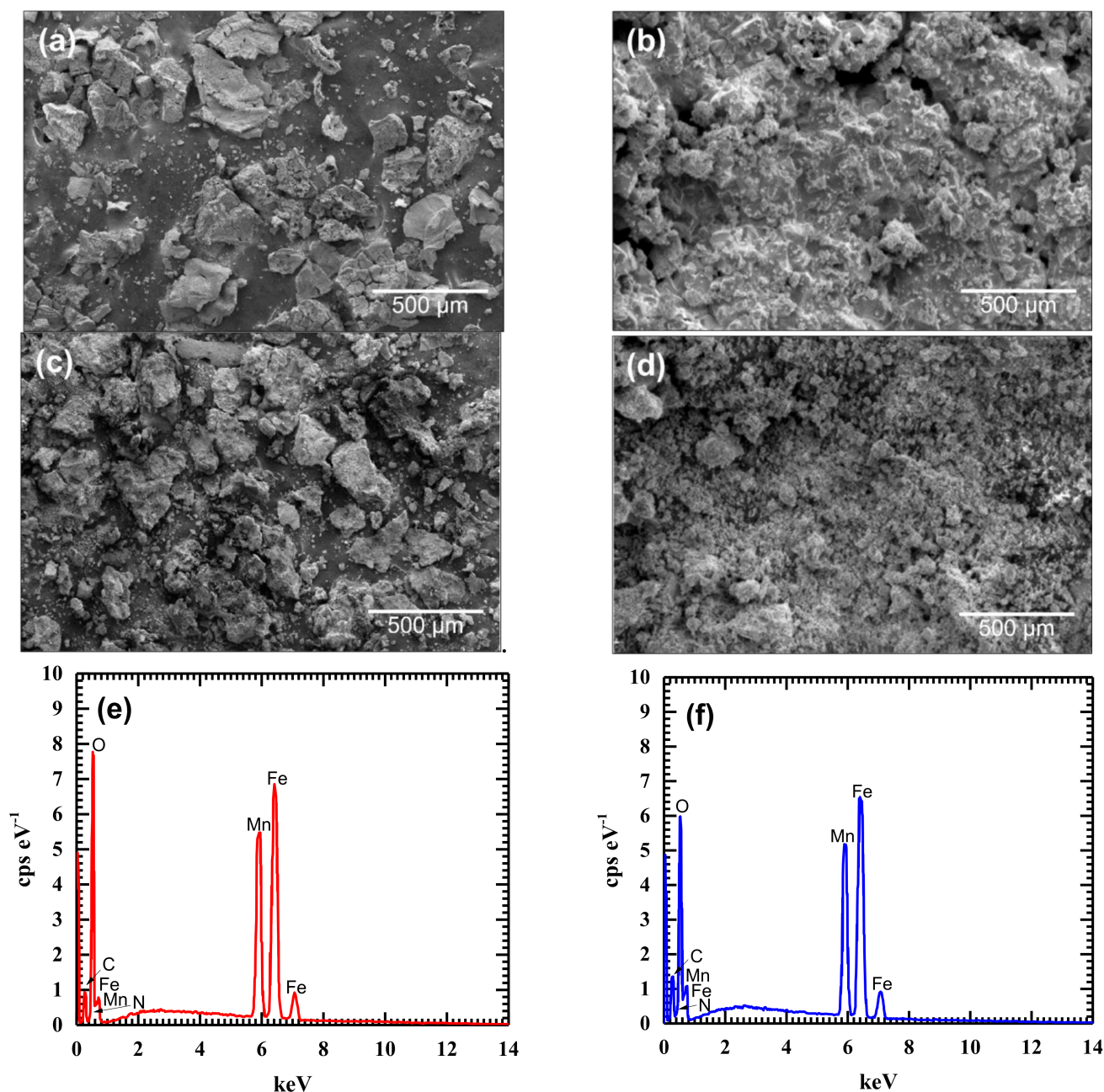


Figure 1. SEM images of (a) MFO taken at 100 \times ; (b) MFO taken at 10,000 \times ; (c) CMFO taken at 100 \times ; and (d) CMFO taken at 10,000 \times magnifications; EDS spectra of (e) MFO and (f) CMFO.

The FTIR spectra of chitosan, MFO, and CMFO were recorded from 400 to 4000 cm^{-1} and are presented in Figure 2a. In the high resolution graph in Figure 2b, each of the curves for chitosan, MFO, and CMFO had a peak at $\sim 2900 \text{ cm}^{-1}$, which pertains to the stretching vibrations of aliphatic C–H bonds [31,35]. The broad bands in the 3200–3500 cm^{-1} region of the CMFO and chitosan curves were due to the hydrogen bonding of $-\text{NH}_2$ and $-\text{OH}$ bonds [37]. In Figure 2c, the formation of new peaks at 1383.68 and 1080.91 cm^{-1} of the CMFO spectrum was noted, indicating that chitosan was successfully coated on the surface of MFO. The peak at 1381.75 cm^{-1} of the chitosan curve confirms the stretching vibration of C–O and $-\text{C}-\text{O}-\text{C}$ (chitosan main chains), while that at 1078.98 cm^{-1} pertains to C–O bond stretching [31,35]. In Figure 2d, the CMFO curve showed the same peaks with MFO at ~ 560 and $\sim 480 \text{ cm}^{-1}$, corresponding to asymmetric C=O, Fe–O, and Mn–O stretching vibration modes, respectively [38].

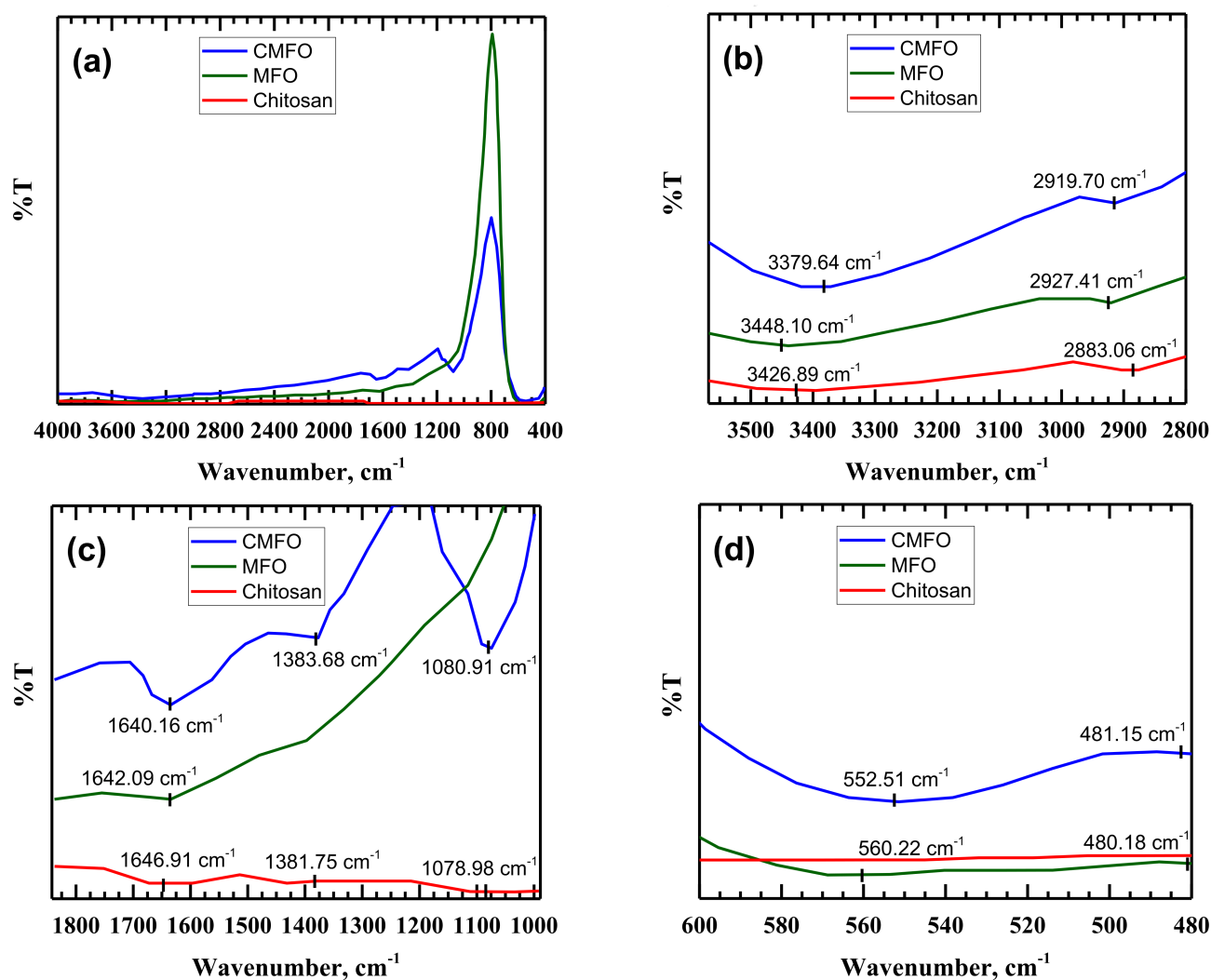


Figure 2. FTIR spectra of CMFO, MFO, and pure chitosan at (a) 400 to 4000 cm^{-1} , (b) 2800 to 3575 cm^{-1} , (c) 1000 to 1825 cm^{-1} , and (d) 480 to 600 cm^{-1} .

3.2. Adsorption Kinetics

The influence of contact time on Cu(II) and Pb(II) uptake by CMFO and MFO is presented in Figure 3 at different temperatures (25, 35, and 45 °C). At any given temperature and time, metal ion uptake by CMFO was consistently higher than MFO, indicating that chitosan enhanced the adsorption performance of MFO. At 25 °C (Figure 3a,b), a rapid increase in adsorption capacity was noted during the first 4 h, which continued to rise gradually until 24 h, after which no significant increase in metal adsorption was recorded. A similar trend was observed at 35 °C (Figure 3c,d), only that enhanced removal of the metal ions extended up to 24 h. As the temperature was further raised to 45 °C (Figure 3e,f), more metals were adsorbed by both MFO and CMFO and no further increase in metal ion removal was detected beyond 24 h of adsorption. Thus, in the subsequent adsorption experiments, 24 h was used as the time required to achieve equilibrium. Meanwhile, the highest amount of adsorbed Cu(II) and Pb(II), equal to 14.86 and 15.36 mg g^{-1} , respectively, were achieved by CMFO, while only 2.59 mg g^{-1} Cu(II) and 13.52 mg g^{-1} Pb(II) were removed by MFO at 45 °C after 24 h.

In each of the operating temperatures considered in this study, Pb(II) exhibited higher affinity than Cu(II) towards both MFO and CMFO. This can be explained by the physico-chemical characteristics of the metal ions (i.e., hydrated ionic radius and electronegativity) and the intrinsic properties of the adsorbent (i.e., type of reactive groups). Previous re-

ports suggested that higher electronegativity and smaller hydrated radius ensure a more favorable adsorption through surface complexation [39]. The electronegativity values of Pb(II) and Cu(II), based on Linus Pauling scale, are 2.33 and 1.90, respectively. Therefore, Pb(II), being more electronegative than Cu(II), has stronger affinity for the lone pair of electrons in the hydroxyl ($-OH$) groups of CMFO and MFO and the amino ($-NH_2$) group of CMFO. Meanwhile, the hydrated ionic radii of Pb(II) and Cu(II) are 0.401 and 0.419 nm, respectively [40]. The smaller the hydrated ionic radius, the nearer it is to the adsorbing surface and the greater its interaction with the oppositely-charged adsorption site; thus, Pb(II) has a higher comparative adsorption capacity than Cu(II).

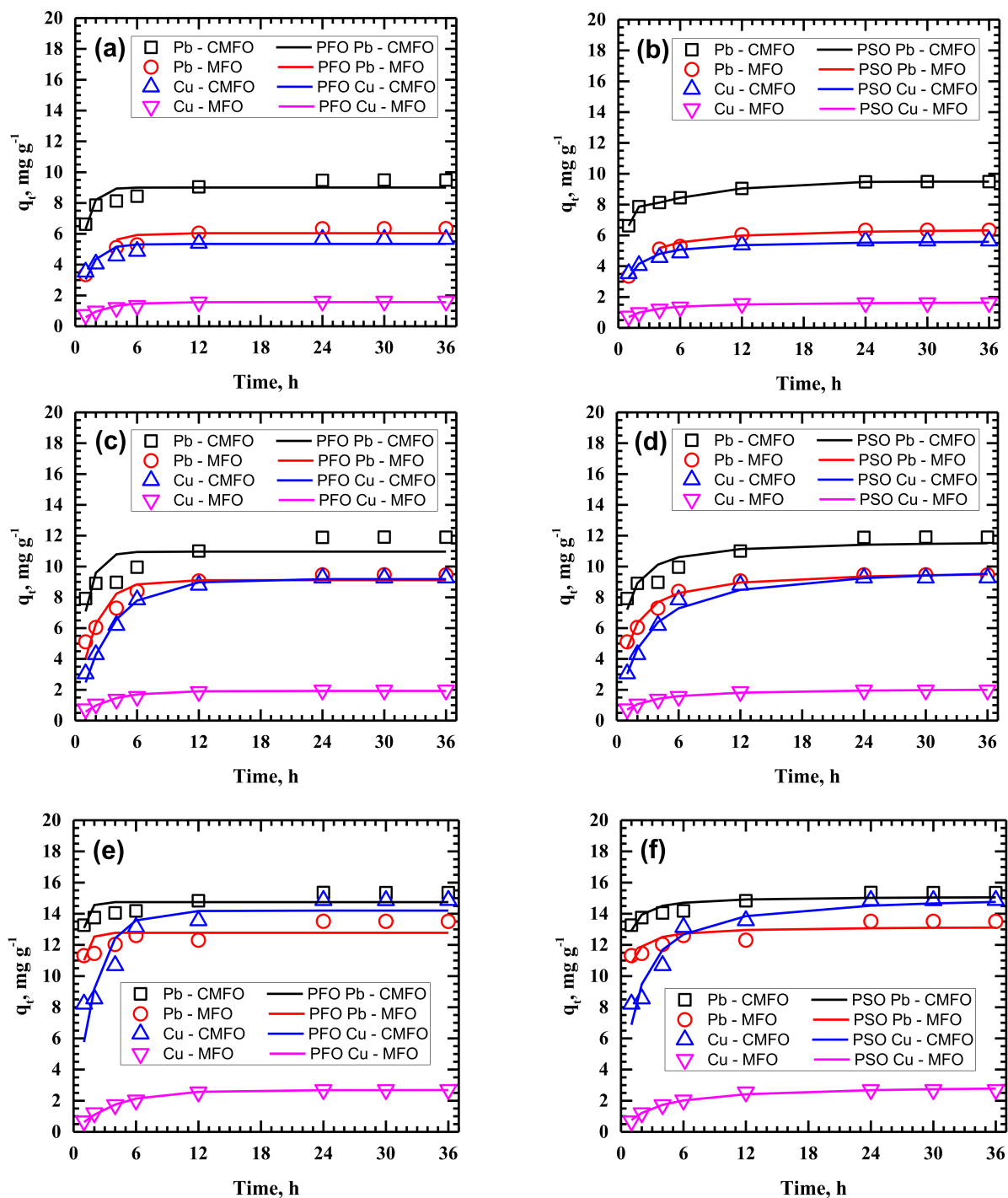


Figure 3. Nonlinear fitting of pseudo-first-order and pseudo-second-order kinetic models for Cu(II) or Pb(II) uptake by CMFO or MFO at different solution temperatures: (a,b) 25 °C, (c,d) 35 °C, and (e,f) 45 °C.

The time dependence of adsorbate interaction with the solid adsorbent is referred to as adsorption kinetics. Studying the kinetics of adsorption for a given system is essential to gain insight into the rate-determining step of the adsorption process. This can be determined by the application of several kinetic models, such as the pseudo-first order (PFO), pseudo-second order (PSO), and intraparticle diffusion models.

The pseudo-first-order model, first proposed by Lagergren [41] in 1898, is a simple kinetic model that assumes physical adsorption as the rate-controlling mechanism in the adsorption system, and is expressed by Equation (2):

$$q_t = q_e \left(1 - e^{-k_1 t}\right) \quad (2)$$

where k_1 is the PFO kinetic constant (min^{-1}), while q_e and q_t are the adsorption capacities (mg g^{-1}) at equilibrium and any time t (min), respectively.

The pseudo-second-order kinetic model, on the other hand, assumes that chemisorption controls the reaction rate [42]. The PSO kinetic equation is given by Equation (3) [43]:

$$q_t = \frac{q_e^2 k_2 t}{1 + k_2 q_e t} \quad (3)$$

where k_2 is the PSO rate constant ($\text{g mg}^{-1} \text{min}^{-1}$); q_t is the adsorption capacity (mg g^{-1}) at time t (min) and q_e is adsorption capacity (mg g^{-1}) at equilibrium.

Unlike the PFO and PSO models, the Weber-Morris intraparticle diffusion model can elucidate the diffusion mechanism of Cu(II) and Pb(II) into the pores of MFO and CMFO. The model equation can be written as Equation (4) [44]:

$$q_t = k_{ip} t^{0.5} + C_i \quad (4)$$

where q_t is the adsorption capacity (mg g^{-1}) at time t (h), k_{ip} , the slope from the plot of q_t versus $t^{0.5}$, is the intraparticle diffusion rate constant ($\text{mg g}^{-1} \text{h}^{-0.5}$); and C_i is the intercept that is proportional to the boundary layer thickness (mg g^{-1}).

Figure 3 also displays the nonlinear plots of PFO and PSO models at 25, 35, and 45 °C. Kinetic parameters for these models and their coefficients of determination (R^2) at each operating temperature are summarized in Table 1. From the results, the PSO model provided excellent and better fit to experimental data at any given temperature than the PFO model on the basis of higher, near-unity R^2 values. Moreover, experimental q_e values for PSO were found to be in very good agreement with the model-predicted q_e values (Table 1). These indicate that chemisorption governs the overall adsorption rate-controlling mechanism, which involves the formation of valence forces between the metal ions and the MFO/CMFO binding sites via the sharing or exchange of electrons [16]. In general, the calculated kinetic rate constant (k_2) of Pb(II) was greater than Cu(II), which signifies that Pb(II) was adsorbed relatively faster than Cu(II). The PSO kinetics also adequately described Cu(II) and Pb(II) adsorption onto various magnetic nanoparticles of previous studies [31,45,46].

The Weber-Morris model plots (q_t vs. $t^{0.5}$) for the experimental kinetic data at varying solution temperatures are depicted in Figure 4. As shown, experimental data for each run can be fitted in two connected lines of different slopes. The bilinear graphs denote the occurrence of two steps involved in the adsorbate transport during the adsorption process [44], namely: film diffusion and intraparticle diffusion represented by the first and second lines, respectively. The generally higher slope of the first line compared to the second ($k_{ip1} > k_{ip2}$) denotes that the transfer of Cu(II) and Pb(II) ions from the solution to the external surface of the adsorbent occurred faster than their diffusion into the internal pore structures of CMFO and MFO. Such information is important as it controls the engineering design [44]. For this model, the kinetic parameters and the corresponding coefficients of determination (R^2) for the uptake of Cu(II) and Pb(II) by the magnetic adsorbents at 25, 35, and 45 °C are also summarized in Table 1.

Table 1. Pseudo-first order, pseudo-second order, and intraparticle diffusion kinetic parameters for Cu(II) and Pb(II) uptake by CMFO and MFO at varying solution temperatures.

Temperature	25 °C				35 °C				45 °C				
Adsorbent	CMFO		MFO		CMFO		MFO		CMFO		MFO		
Metal	Cu	Pb	Cu	Pb	Cu	Pb	Cu	Pb	Cu	Pb	Cu	Pb	
q_e exp	5.649	9.472	1.622	6.337	9.263	11.887	1.971	9.46	14.861	15.358	2.587	13.515	
PFO	k_1	0.014	0.0202	0.0078	0.0111	0.0052	0.0173	0.006	0.0097	0.0087	0.0363	0.0044	0.0329
	R^2	0.7529	0.7439	0.9126	0.8465	0.9877	0.5419	0.9537	0.8696	0.7959	0.4447	0.9931	0.3693
	q_e	5.345	9.007	1.571	6.04	9.185	10.964	1.925	9.117	14.2	14.747	2.681	12.779
PSO	k_2	0.004	0.0039	0.0069	0.0025	0.0007	0.0023	0.0041	0.0016	0.0009	0.0065	0.0019	0.0058
	R^2	0.9571	0.9465	0.9892	0.9847	0.9842	0.8382	0.9943	0.9779	0.9258	0.7982	0.9921	0.7212
	q_e	5.697	9.459	1.698	6.501	10.155	11.71	2.107	9.774	15.256	15.126	3.006	13.192
ID	k_{ip1}	0.7416	0.8672	0.3234	1.0690	2.4165	1.1922	0.4447	1.6458	2.4546	0.5926	0.7394	0.4738
	C_{i1}	2.9530	6.2287	0.5009	2.5678	1.0413	6.8871	0.4048	3.7799	5.7577	12.7914	0.1162	10.9599
	R^2	0.9639	0.8562	0.9627	0.9208	0.9358	0.9555	0.9642	0.9372	0.8872	0.9712	0.9644	0.6839
	k_{ip2}	0.1064	0.1852	0.0232	0.1222	0.1970	0.3770	0.0418	0.1673	0.5397	0.2140	0.0608	0.5037
	C_{i2}	5.0592	8.4550	1.4921	5.6587	8.1680	9.8019	1.7383	8.5318	11.8592	14.1589	2.3615	10.7103
R^2	0.8340	0.8566	0.8325	0.8338	0.8342	0.8401	0.8274	0.8345	0.8327	0.8159	0.8284	0.8273	

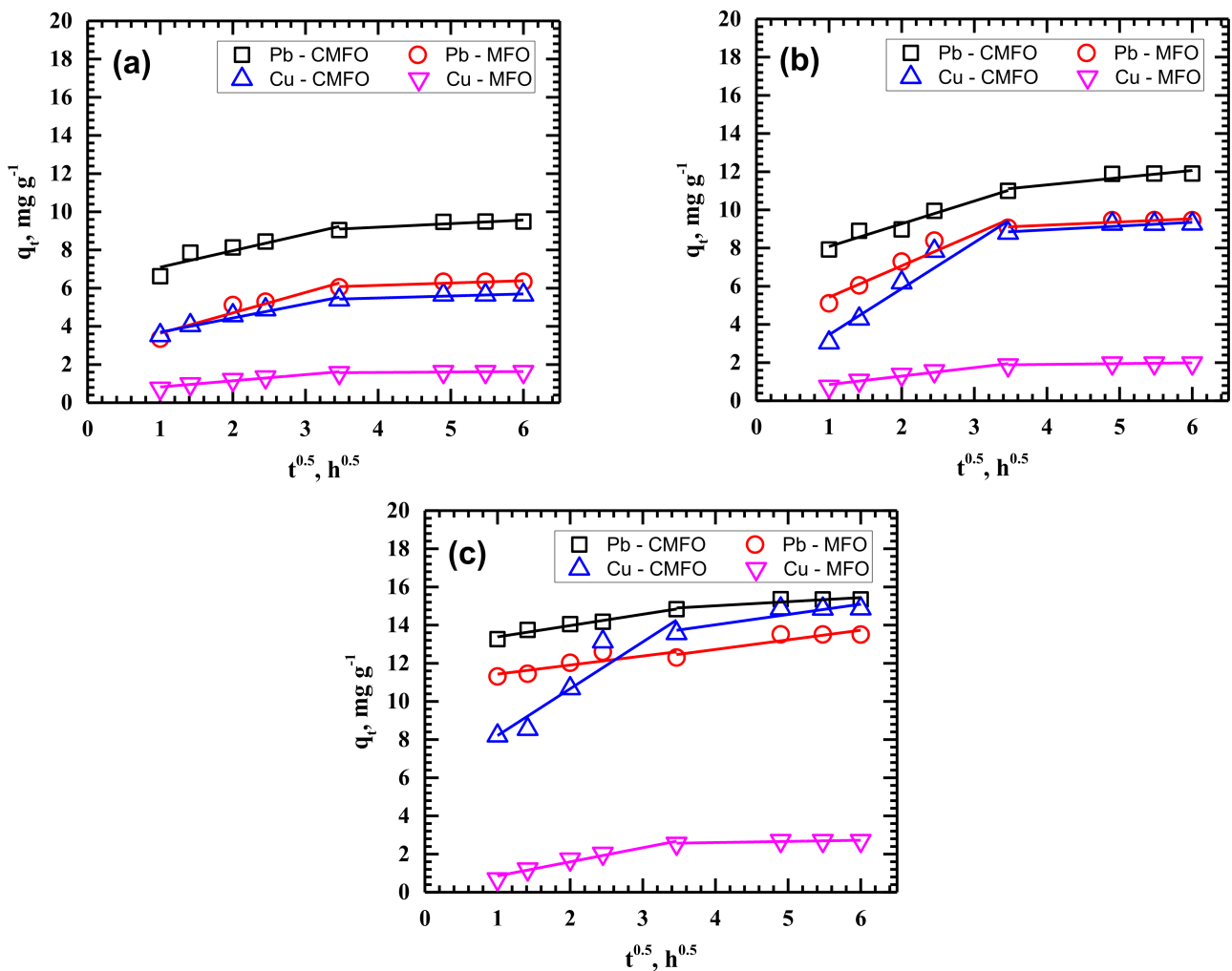


Figure 4. Intraparticle diffusion plots for Cu(II) and Pb(II) uptake by CMFO or MFO at varying solution temperatures: (a) 25 °C, (b) 35 °C, and (c) 45 °C.

3.3. Adsorption Thermodynamics

In Figure 5a, the adsorption capacities of CMFO or MFO for Cu(II) or Pb(II) improved significantly as the temperature was raised from 25 to 45 °C. At 45 °C, CMFO adsorbed 14.9 mg g⁻¹ Cu(II) and 15.4 mg g⁻¹ Pb(II), while MFO adsorbed 2.6 mg g⁻¹ Cu(II) and 13.5 mg g⁻¹ Pb(II). When compared to the experimental q_e values obtained at 25 °C (see Table 1), the above mentioned values are equivalent to an enhancement of 163% and 62% for Cu(II) and Pb(II) removal by CMFO and 60% and 113% of Cu(II) and Pb(II) uptake by MFO, respectively.

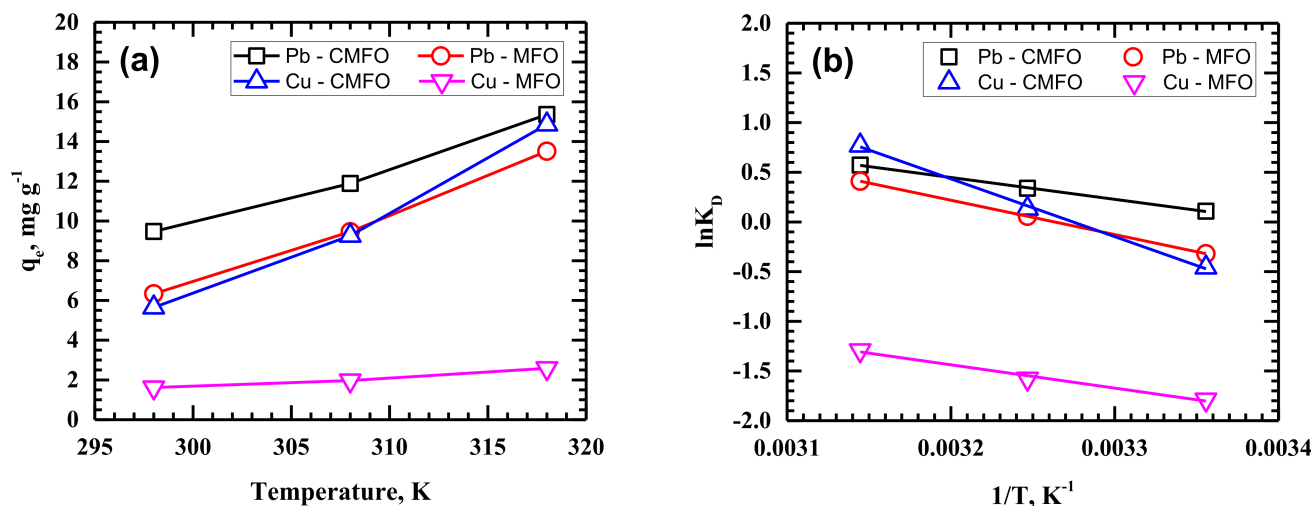


Figure 5. (a) Effect of temperature on the uptake of Cu(II) and Pb(II) by CMFO and MFO and (b) thermodynamic plot of $\ln K_D$ against $1/T$ of Cu(II) and Pb(II) uptake on CMFO and MFO.

Adsorption capacity of an adsorbent may increase or decrease at higher temperatures, depending on the nature of the reaction process. The temperature of the adsorption medium could be significant for energy-driven mechanisms in the metal uptake of sorbents. If the reaction is endothermic, then adsorption may be enhanced at higher temperatures. Where the reaction is exothermic, a decline in adsorption with increasing temperature will be noted. To assess the nature of the adsorption process, thermodynamic parameters such as Gibb's free energy change (ΔG°), enthalpy change (ΔH°), and entropy change (ΔS°) were computed using Equations (5) and (6) [47]:

$$\Delta G^\circ = -RT \ln k_C \quad (5)$$

$$k_C = \frac{q_e}{C_e} \times 1000 \quad (6)$$

where k_C (dimensionless) is the equilibrium constant derived from the distribution coefficient ($k_D = q_e/C_e$) multiplied by 1000 [48]; q_e is the equilibrium metal adsorption capacity (mg g⁻¹); C_e is the amount of metal remaining in the solution (mg L⁻¹) at equilibrium; R is the universal gas constant (8.314 J mol⁻¹ K⁻¹); and T is the absolute temperature (K). The values of ΔH° and ΔS° can be obtained using the Van't Hoff equation in Equation (7):

$$\ln k_C = \frac{\Delta S^\circ}{R} - \frac{\Delta H^\circ}{RT} \quad (7)$$

Consequently, the slope and intercept of the plot between $\ln k_C$ and $1/T$ (Van't Hoff plot) in Figure 5b, was used to determine the values of ΔH° (kJ mol⁻¹) and ΔS° (kJ mol⁻¹ K⁻¹), respectively. In Table 2, the uptake of metal ions by CMFO and MFO resulted in negative ΔG° values, signifying that the adsorption of Pb(II) and Cu(II) was spontaneous [49]. Between the two metal ions, more negative ΔG° values were noted for Pb(II), indicating a more spontaneous and more energetically favorable sorption mecha-

nism, which explains why the adsorption capacity of CMFO and MFO for Pb(II) was higher than Cu(II) [39]. Increasing the temperature resulted in more negative values of ΔG° , suggesting that the reaction became more spontaneous at higher temperatures [49]. This was validated by the positive value of ΔH° , signifying that the reaction was endothermic; hence raising the temperature resulted in the enhancement in adsorption capacity [39]. Moreover, enthalpy values (18.28–48.33 kJ mol⁻¹) specified that the adsorption process of Cu(II) and Pb(II) onto CMFO and MFO proceeded by way of chemical interaction [47], confirming the results in adsorption kinetics. Lastly, the positive values of ΔS° suggest a dissociative adsorption mechanism and an increase in randomness at the solid-solution interfaces as a result of the splitting of water from hydrated Cu(II) or Pb(II) upon attachment to the surface of CMFO and MFO [47].

Table 2. Thermodynamic parameters on the adsorption capacity of CMFO and MFO.

Adsorbate	Temperature (°C)	MFO				CMFO			
		ΔG° (kJ mol ⁻¹)	ΔH° (kJ mol ⁻¹)	ΔS° (kJ mol ⁻¹ K ⁻¹)	R ²	ΔG° (kJ mol ⁻¹)	ΔH° (kJ mol ⁻¹)	ΔS° (kJ mol ⁻¹ K ⁻¹)	R ²
Pb	25	-16.32	28.75	0.151	0.9999	-17.38	18.28	0.120	0.9995
	35	-17.84				-18.57			
	45	-19.35				-19.77			
Cu	25	-12.65	19.49	0.108	0.9888	-15.95	48.33	0.216	0.9985
	35	-13.73				-18.10			
	45	-14.81				-20.26			

3.4. Adsorption Isotherms

Adsorption isotherms determine the adsorption capacity of solutes at equilibrium. The sorbate-sorbent interaction between Cu(II) or Pb(II) and the prepared magnetic adsorbents was quantitatively determined via the nonlinear fitting of various isotherm models (i.e., Langmuir, Freundlich, Temkin, and Dubinin–Radushkevich) onto the equilibrium batch experimental data.

The Langmuir isotherm has been widely used by many authors to explain the sorption of heavy metals onto biosorbents, metal oxides, magnetic nanoparticles, clay, soils, etc. Langmuir isotherm explains the sorbate-sorbent interaction based on the assumption that only one layer (monolayer) of the sorbate molecules can attach to a specific number of active sites on the surface of the adsorbent [50]. The Langmuir isotherm model is represented by Equation (8) [50]:

$$q_e = \frac{K_L C_e q_{max}}{1 + K_L C_e} \quad (8)$$

where C_e and q_e are the equilibrium metal ion concentration (mg L⁻¹) and equilibrium adsorption capacity (mg g⁻¹), respectively, while q_{max} is the maximum adsorption capacity (mg g⁻¹). K_L refers to the Langmuir constant (L mg⁻¹), and is used to calculate the dimensionless separation factor (R_L) given by Equation (9) [18]:

$$R_L = \frac{1}{1 + K_L C_o} \quad (9)$$

where C_o is the initial metal ion concentration (mg L⁻¹).

An alternate isotherm frequently used to model lower adsorbate concentration is the Freundlich isotherm. It is based on the principle that the adsorbent surface is heterogeneous and a non-uniform distribution of the heat of adsorption exists on the adsorbent surface [51]. The Freundlich equation may be written as Equation (10) [51]:

$$q_e = K_F (C_e)^{\frac{1}{n}} \quad (10)$$

where K_F refers to the adsorption capacity of the adsorbent (mg g⁻¹), and $1/n$ signifies the intensity of the adsorption.

Meanwhile, the Temkin isotherm is actually an extension of the Langmuir isotherm that assumes that the adsorbate-adsorbent interactions may cause the adsorption enthalpy to decrease linearly with coverage [52]. The Temkin equation may be expressed as Equation (11) [52]:

$$q_e = B_T \ln(A_T C_e) \quad (11)$$

where $B_T = \frac{RT}{b}$ is the Temkin constant equal to the product of universal gas constant (R , $8.314 \text{ J}\cdot\text{mol}^{-1} \text{ K}^{-1}$) and absolute temperature (T , K) divided by the heat of adsorption (b , J mol^{-1}), and A_T is the equilibrium binding constant (L g^{-1}).

The Dubinin–Radushkevich model recognizes the characteristics of the adsorbent porosity and the apparent sorption energy [53]. The D-R equation is given in Equation (12):

$$q_e = q_D \exp[-\beta \epsilon^2] \quad (12)$$

where q_e is the equilibrium adsorption capacity (mg g^{-1}), q_D is the Dubinin–Radushkevich constant that describes the degree of adsorption, β is the activity coefficient that provides the sorption mean energy ($\text{mol}^2 \text{ kJ}^{-2}$), and ϵ^2 is the Polanyi potential that can be computed using Equation (13):

$$\epsilon = RT \ln\left(1 + \frac{1}{C_e}\right) \quad (13)$$

Figure 6a–d show the nonlinear fitting of Langmuir, Freundlich, Temkin, and D-R isotherm models, respectively, for the Cu(II) and Pb(II) uptake by CMFO and MFO. The isotherm model parameters are listed in Table 3. Based on the figures and the values of the coefficients of determination (R^2), it shows that the Langmuir model best described the adsorption of Cu(II) and Pb(II) onto CMFO and MFO compared to other isotherm models. A better fit onto the Langmuir model denotes that the adsorption favors monolayer coverage and interaction among the adsorbed metal ions was negligible. The values of the Langmuir isotherm parameters q_m and K_L of Pb(II) were greater than Cu(II) for both CMFO and MFO, which means Pb(II) had greater affinity to the surface functional groups of both adsorbents than Cu(II). Furthermore, the favorability of adsorption can be distinguished via the separation factor, R_L . Depending upon the computed R_L values, the adsorption can be described as unfavorable if $R_L > 1$, linear if $R_L = 1$, favorable if $0 < R_L < 1$, or irreversible if $R_L = 0$. As seen in Table 3, the R_L values at 25 to 200 mg L^{-1} Pb(II) for CMFO (0.03 to 0.19) and MFO (0.05 to 0.30), and Cu(II) for CMFO (0.25 to 0.73) and MFO (0.14 to 0.57) denote that the adsorption was favorable. Thus, the two synthesized magnetic adsorbents can be used as suitable adsorbents for the uptake of Cu(II) and Pb(II) ions.

Table 3. Isotherm model parameters for the uptake of Cu(II) or Pb(II) by CMFO or MFO.

Adsorption Isotherm	Parameters	CMFO		MFO	
		Cu	Pb	Cu	Pb
Langmuir	q_{max}	8.0970	9.7250	1.8720	6.6911
	K_L	0.0146	0.1726	0.0307	0.0945
	R_L	0.25–0.73	0.03–0.19	0.14–0.57	0.05–0.30
	R^2	0.9774	0.9977	0.9912	0.9988
Freundlich	n	2.0965	5.9625	3.1984	5.1734
	K_F	0.5120	4.2435	0.3222	2.4413
	R^2	0.9436	0.8718	0.9773	0.9066
Temkin	B_T	1.8575	1.3615	0.3897	1.0450
	A_T	0.1307	8.9403	0.3496	3.1112
	R^2	0.9717	0.9231	0.9958	0.9488
D-R	q_D	5.1952	8.8887	1.4775	5.9577
	β	1.02×10^{-4}	3.98×10^{-6}	6.10×10^{-5}	1.31×10^{-5}
	R^2	0.8081	0.9258	0.8370	0.9161

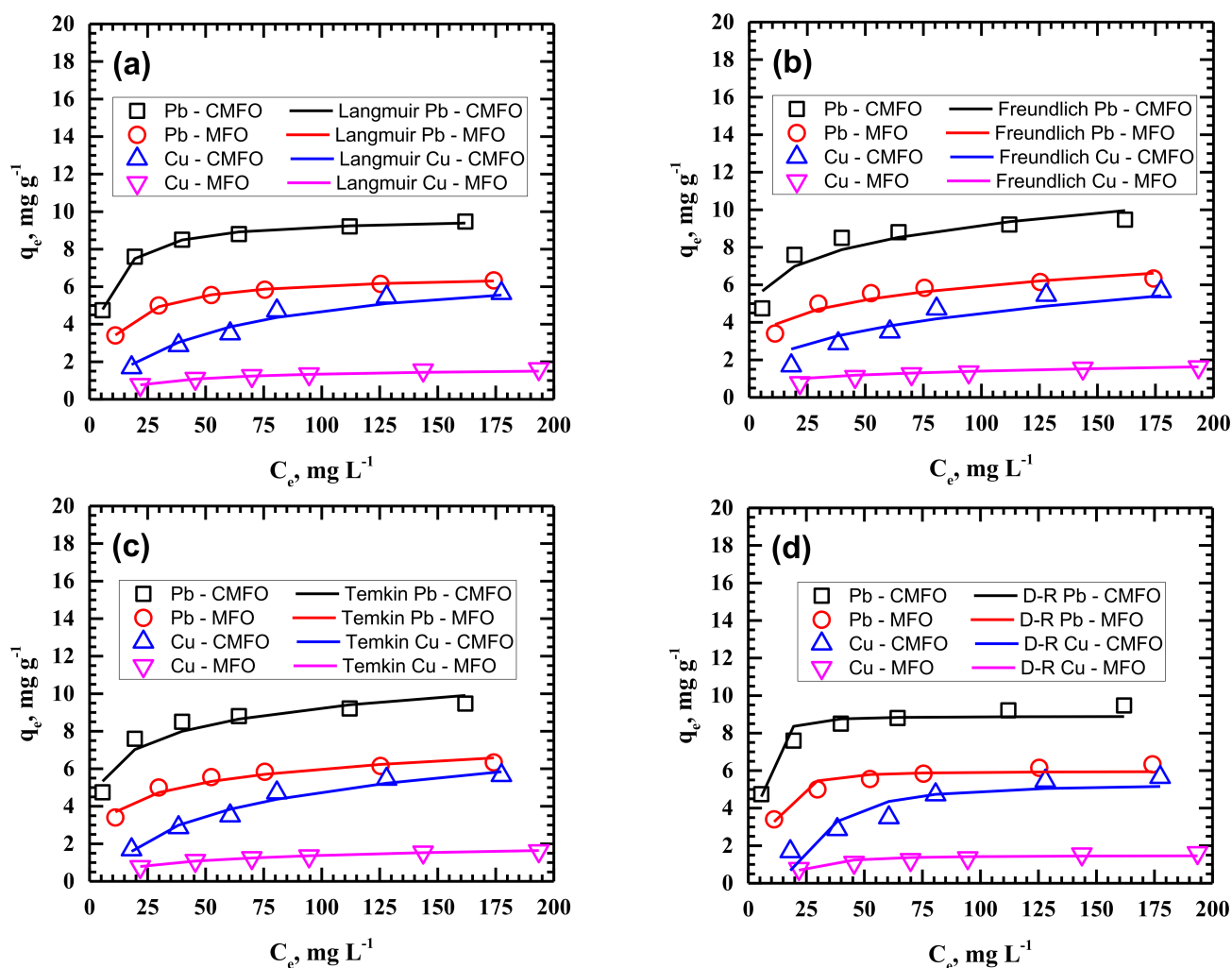


Figure 6. Nonlinear fitting of (a) Langmuir, (b) Freundlich, (c) Temkin, and (d) D-R isotherm models of Cu(II) and Pb(II) uptake by CMFO and MFO.

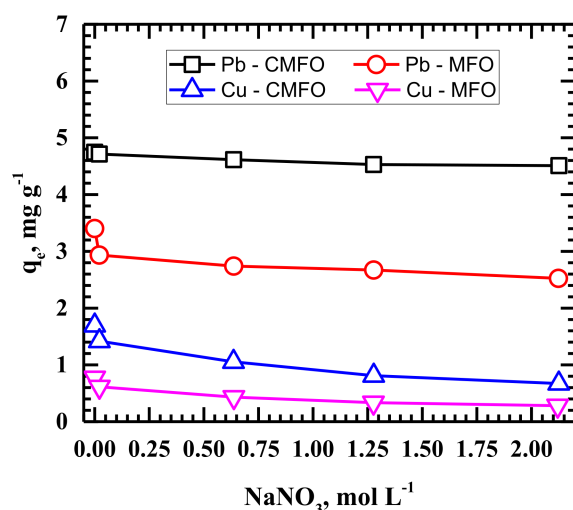
Table 4 summarizes the adsorptive performances of various MFO-based nanoadsorbents for Cu(II) and Pb(II), including the results of the present study. As shown, some experimental q_e values by previous reports exceeded those of the present study. The discrepancies are due in part to the variations in experimental conditions during adsorbent synthesis and the operating conditions in the adsorption experiments. For example, solution pH was varied and optimized in previous studies, while in the present study the pH was only set to 4.5 in all experiments to simulate the typical Cu(II)- and Pb(II)-laden wastewater pH which ranges from pH 4–6. Adsorption is highly dependent on the pH of the water matrix due to the electrostatic attraction or repulsion with H^+ or OH^- ions on the adsorbent surface. It is therefore recommended that in future studies, critical parameters during adsorbent synthesis and those for adsorption experiments such as solution pH, temperature, and adsorbent dosage should be optimized to improve the maximum capacity of the adsorbent material.

Table 4. Adsorptive performances of various MFO-based nanoadsorbents for Cu(II) and Pb(II).

Metal Ions	Magnetic Nanosorbents	Experimental Conditions *	q_e (mg g ⁻¹)	Reference
Cu(II)	MnFe ₂ O ₄	m = 0.1 g L ⁻¹ ; pH = 4.5; T = 45 °C; t = 24 h	2.59	This study
	Chitosan-coated MnFe ₂ O ₄	m = 0.1 g L ⁻¹ ; pH = 4.5; T = 45 °C; t = 24 h	14.86	This study
	Chitosan-coated MnFe ₂ O ₄	m = 0.03 g L ⁻¹ ; pH = 6; T = 20 °C; t = 6 h	22.6	[31]
	MnFe ₂ O ₄	m = 1 g L ⁻¹ ; pH = 6; T = 25 ± 2 °C; t = 3 h	60.5	[45]
	Chitosan-coated MnFe ₂ O ₄	m = 3.33 g L ⁻¹ ; pH = 6.5; T = 20 °C; t = 8.33 h	65.1	[54]
	MnFe ₂ O ₄	m = 2 g L ⁻¹ ; pH = 5; t = 2 h	43.02	[55]
Pb(II)	MnFe ₂ O ₄	m = 0.1 g L ⁻¹ ; pH = 4.5; T = 45 °C; t = 24 h	13.52	This study
	Chitosan-coated MnFe ₂ O ₄	m = 0.1 g L ⁻¹ ; pH = 4.5; T = 45 °C; t = 24 h	15.36	This study
	MnFe ₂ O ₄	m = 0.8 g L ⁻¹ ; pH = N.S.; T = 20 °C; t = 1 h	8.3	[56]
	MnFe ₂ O ₄	m = 1 g L ⁻¹ ; pH = 6.8 ± 0.4; T = N.S.; t = 24 h	5.2	[57]
	MnFe ₂ O ₄	m = 1 g L ⁻¹ ; pH = 6; T = 25 ± 2 °C; t = 3 h	69.1	[45]

* m = adsorbent dosage, T = solution temperature, t = contact time, N.S. = not specified.

In natural waters, the ionic strength or the concentration of salt species co-existing with target heavy metal ions may affect the metal removal capacity of adsorbents. In this study, the highest adsorption capacities of CMFO and MFO for Cu(II) and Pb(II) were recorded when no NaNO₃ was added to each metal solution (see Figure 7). In the presence of 0.02 mol L⁻¹ NaNO₃, however, CMFO adsorption capacities dropped by 16.28% and 0.65% for Cu(II) and Pb(II), respectively. Using the same salt concentration, MFO metal uptake was reduced by 20.77% for Cu(II) and 13.75% for Pb(II). Increasing NaNO₃ concentration by a hundredfold from 0.02 to 2.12 mol L⁻¹ resulted in a slight decline in the uptake for Pb(II) (i.e., 4.32% using CMFO and 13.94% using MFO) but a drastic reduction for Cu(II) (i.e., 52.64% using CMFO and 54.34% using MFO). Clearly, the negative effect of ionic strength was consistently greater for Cu(II) and MFO than Pb(II) and CMFO.

**Figure 7.** Effect of salt concentration on the uptake of Cu(II) and Pb(II) by CMFO and MFO.

The effect of ionic strength on metal uptake can be attributed to (1) the competition between the target heavy metal ion and the salt ions for available binding sites on the adsorbent surface, and (2) the formation of metal complexes between the target heavy metal and the anion from the supporting electrolyte due to electrostatic interaction [58]. The lower ionic-strength effect with CMFO compared to MFO is indicative of the improved adsorptive potential of CMFO ascribed to chitosan-coating, which provided more binding sites for metal uptake. Meanwhile, adsorption of Cu(II) and Pb(II) was reduced in the presence of dissolved NaNO₃ mainly because Na⁺ and NO₃⁻ have a smaller hydrated ionic radius of 0.36 and 0.34 nm, respectively, which enabled them to readily attach to

the adsorbent surface functional groups [59]. In addition, NO_3^- had a more inhibitory effect on metal adsorption compared to Na^+ since the anion can form complexes with heavy metal ions [60]. Pb(II), however, does not readily form a stable complex with NO_3^- , hence the negligible decline in Pb(II) uptake was noted at higher ionic strength [61]. The lower ionic-strength effect noted for Pb(II) compared to Cu(II) can also be explained by the higher electronegativity and smaller hydrated ionic radius of the former, which contribute to the formation of the inner sphere complex between the Pb(II) ions and the functional groups on the adsorbent surface through chemical bonds (i.e., covalent and ionic). On the other hand, outer-sphere complexes implicate weak electrostatic attraction and are greatly affected by the ionic strength of the solution, as may be the case for Cu(II). Similar results were obtained by previous studies involving the adsorption of copper and lead by cubic spinel-type MnFe_2O_4 /biochar [58] and MnFe_2O_4 @alunite composite [62].

4. Conclusions

The present study has successfully demonstrated the adsorptive potential of MFO and CMFO, synthesized by the low-temperature combustion technique, for the uptake of Cu(II) or Pb(II) from a contaminated solution. The presence of additional binding sites in CMFO led to higher adsorption capacities for Cu(II) and Pb(II) when compared to MFO, with Pb(II) having a higher affinity for both synthesized adsorbents. The kinetics on the uptake of Cu(II) or Pb(II) onto CMFO and MFO showed an excellent fit for the pseudo-second order model indicating that chemisorption is the rate-determining step of the adsorption process. Better fit of equilibrium data to Langmuir model denotes that monolayer adsorption was favored. The adsorption capacity of CMFO and MFO improved as the solution temperature was increased, with the endothermic reaction validated by positive values of ΔH° . The uptake of Cu(II) and Pb(II) onto CMFO and MFO was spontaneous, as denoted by the negative ΔG° values, and the positive values of ΔS° indicated an increased randomness of the solution at the solid-solution interface. The adsorption capacity of MFO and CMFO decreased with increasing salt concentration. The present study has demonstrated the applicability of chitosan-manganese ferrite composite and manganese ferrite, prepared through the low-temperature combustion technique, in adsorbing heavy metals like copper and lead ions. Additional experiments on the effects of pH and higher temperatures on metal uptake by CMFO, as well as optimization of relevant experimental parameters should be considered in future studies to further improve the adsorption performance of the magnetic adsorbent.

Author Contributions: Conceptualization, M.D.G.d.L., C.-C.K., and N.G.; methodology, M.A.M.T. and D.C.O.; software, M.A.M.T., D.C.O., and B.M.B.E.; validation, B.M.B.E., D.C.O., and C.-C.K.; formal analysis, B.M.B.E., M.A.M.T., and D.C.O.; investigation, M.A.M.T., N.G., and J.-J.Y.; resources, M.D.G.d.L., C.-C.K., and N.G.; data curation, M.A.M.T. and D.C.O.; writing—original draft preparation, M.A.M.T., D.C.O., and B.M.B.E.; writing—review and editing, B.M.B.E., D.C.O., and M.D.G.d.L.; visualization, D.C.O.; supervision, M.D.G.d.L., C.-C.K., and J.-J.Y.; project administration, M.D.G.d.L., C.-C.K., and J.-J.Y.; funding acquisition, M.D.G.d.L., C.-C.K., and J.-J.Y. All authors have read and agreed to the published version of the manuscript.

Funding: This research was funded by the Ministry of Science and Technology, Taiwan (Contract No. MOST-102-2221-E-041-005), the National Research Foundation through the Korea Ministry of Education (No. 2016R1A6A1A03012812), and the Department of Science and Technology, Philippines.

Institutional Review Board Statement: Not Applicable.

Informed Consent Statement: Not Applicable.

Data Availability Statement: Data are contained within the article.

Conflicts of Interest: The authors declare no conflict of interest.

References

1. Viriyatum, R.; Boyd, C.E. Slow-Release Coated Copper Sulfate as an Algicide for Aquaculture. *J. World Aquac. Soc.* **2016**, *47*, 667–675. [\[CrossRef\]](#)
2. Kholghi Eshkalak, S.; Khatibzadeh, M.; Kowsari, E.; Chinnappan, A.; Ramakrishna, S. A Novel Surface Modification of Copper (II) Phthalocyanine with Ionic Liquids as Electronic Ink. *Dye. Pigment.* **2018**, *154*, 296–302. [\[CrossRef\]](#)
3. Isahak, W.N.R.W.; Hasan, S.Z.; Ramli, Z.A.C.; Ba-Abbad, M.M.; Yarmo, M.A. Enhanced Physical and Chemical Adsorption of Carbon Dioxide Using Bimetallic Copper–Magnesium Oxide/Carbon Nanocomposite. *Res. Chem. Intermed.* **2018**, *44*, 829–841. [\[CrossRef\]](#)
4. Rihel, J. Copper on the Brain. *Nat. Chem. Biol.* **2018**, *14*, 638–639. [\[CrossRef\]](#)
5. Kumar, J.; Sathua, K.B.; Flora, S.J.S. Chronic Copper Exposure Elicit Neurotoxic Responses in Rat Brain: Assessment of 8-Hydroxy-2-Deoxyguanosine Activity, Oxidative Stress and Neurobehavioral Parameters. *Cell. Mol. Biol.* **2019**, *65*, 27–35. [\[CrossRef\]](#)
6. Kumar, A.; Cabral-Pinto, M.; Kumar, A.; Kumar, M.; Dinis, P.A. Estimation of Risk to the Eco-Environment and Human Health of Using Heavy Metals in the Uttarakhand Himalaya, India. *Appl. Sci.* **2020**, *10*, 7078. [\[CrossRef\]](#)
7. Marques, D.M.; Veroneze Júnior, V.; da Silva, A.B.; Mantovani, J.R.; Magalhães, P.C.; de Souza, T.C. Copper Toxicity on Photosynthetic Responses and Root Morphology of *Hymenaea Courbaril* L. (Caesalpinioideae). *WaterAirSoil Pollut.* **2018**, *229*, 1–14. [\[CrossRef\]](#)
8. Kumar, A.; Kumar, A.M.M.S.C.-P.; Chaturvedi, A.K.; Shabnam, A.A.; Subrahmanyam, G.; Mondal, R.; Gupta, D.K.; Malyan, S.K.; Kumar, S.S.; Khan, S.A.; et al. Lead Toxicity: Health Hazards, Influence on Food Chain, and Sustainable Remediation Approaches. *Int. J. Environ. Res. Public Health* **2020**, *17*, 2179. [\[CrossRef\]](#)
9. De Luna, M.D.G.; Bellotindos, L.M.; Asiao, R.N.; Lu, M.C. Removal and Recovery of Lead in a Fluidized-Bed Reactor by Crystallization Process. *Hydrometallurgy* **2015**, *155*, 6–12. [\[CrossRef\]](#)
10. García-Lestón Julia, J.; Méndez, J.; Pávaro, E.; Laffon, B. Genotoxic Effects of Lead: An Updated Review. *Environ. Int.* **2010**, *36*, 623–636. [\[CrossRef\]](#)
11. Liao, L.M.; Friesen, M.C.; Xiang, Y.-B.; Cai, H.; Koh, D.-H.; Ji, B.-T.; Yang, G.; Li, H.-L.; Locke, S.J.; Rothman, N.; et al. Occupational Lead Exposure and Associations with Selected Cancers: The Shanghai Men’s and Women’s Health Study Cohorts. *Environ. Health Perspect.* **2016**, *124*, 97–103. [\[CrossRef\]](#)
12. Mitra, P.; Sharma, S.; Purohit, P.; Sharma, P. Clinical and Molecular Aspects of Lead Toxicity: An Update. *Crit. Rev. Clin. Lab. Sci.* **2017**, *54*, 506–528. [\[CrossRef\]](#)
13. Harvey, P.J.; Handley, H.K.; Taylor, M.P. Widespread Copper and Lead Contamination of Household Drinking Water, New South Wales, Australia. *Environ. Res.* **2016**, *151*, 275–285. [\[CrossRef\]](#)
14. Abedi Sarvestani, R.; Aghasi, M. Health Risk Assessment of Heavy Metals Exposure (Lead, Cadmium, and Copper) through Drinking Water Consumption in Kerman City, Iran. *Environ. Earth Sci.* **2019**, *78*, 1–11. [\[CrossRef\]](#)
15. Ong, D.C.; de Luna, M.D.G.; Pingul-Ong, S.M.B.; Kan, C.C. Manganese and Iron Recovery from Groundwater Treatment Sludge by Reductive Acid Leaching and Hydroxide Precipitation. *J. Environ. Manag.* **2018**, *223*, 723–730. [\[CrossRef\]](#)
16. De Luna, M.D.G.; Flores, E.D.; Cenia, M.C.B.; Lu, M.-C. Removal of Copper Ions from Aqueous Solution by Adlai Shell (*Coix Lacryma-Jobi* L.) Adsorbents. *Bioresour. Technol.* **2015**, *192*, 841–844. [\[CrossRef\]](#)
17. Tsai, W.C.; De Luna, M.D.G.; Bermillo-Arriesgado, H.L.P.; Futralan, C.M.; Colades, J.I.; Wan, M.W. Competitive Fixed-Bed Adsorption of Pb(II), Cu(II), and Ni(II) from Aqueous Solution Using Chitosan-Coated Bentonite. *Int. J. Polym. Sci.* **2016**, *2016*. [\[CrossRef\]](#)
18. De Castro, M.L.F.A.; Abad, M.L.B.; Sumalinog, D.A.G.; Abarca, R.R.M.; Paoprasert, P.; de Luna, M.D.G. Adsorption of Methylene Blue Dye and Cu(II) Ions on EDTA-Modified Bentonite: Isotherm, Kinetic and Thermodynamic Studies. *Sustain. Environ. Res.* **2018**, *28*, 197–205. [\[CrossRef\]](#)
19. Tumamos, S.B.; Ensano, B.M.B.; Pingul-Ong, S.M.B.; Ong, D.C.; Kan, C.-C.; Yee, J.-J.; de Luna, M.D.G. Isotherm, Kinetics and Thermodynamics of Cu(II) and Pb(II) Adsorption on Groundwater Treatment Sludge-Derived Manganese Dioxide for Wastewater Treatment Applications. *Int. J. Environ. Res. Public Health* **2021**, *18*, 3050. [\[CrossRef\]](#)
20. Yang, L.X.; Wang, F.; Meng, Y.F.; Tang, Q.H.; Liu, Z.Q. Fabrication and Characterization of Manganese Ferrite Nanospheres as a Magnetic Adsorbent of Chromium. *J. Nanomater.* **2013**, *2013*. [\[CrossRef\]](#)
21. Aryee, A.A.; Mpatani, F.M.; Du, Y.; Kani, A.N.; Dovi, E.; Han, R.; Li, Z.; Qu, L. Fe₃O₄ and Iminodiacetic Acid Modified Peanut Husk as a Novel Adsorbent for the Uptake of Cu (II) and Pb (II) in Aqueous Solution: Characterization, Equilibrium and Kinetic Study. *Environ. Pollut.* **2021**, *268*, 115729. [\[CrossRef\]](#)
22. Behbahani, E.S.; Dashtian, K.; Ghaedi, M. Fe₃O₄-FeMoS₄: Promise Magnetite LDH-Based Adsorbent for Simultaneous Removal of Pb (II), Cd (II), and Cu (II) Heavy Metal Ions. *J. Hazard. Mater.* **2021**, *410*, 124560. [\[CrossRef\]](#) [\[PubMed\]](#)
23. Tran, C.V.; Quang, D.V.; Nguyen Thi, H.P.; Truong, T.N.; La, D.D. Effective Removal of Pb(II) from Aqueous Media by a New Design of Cu–Mg Binary Ferrite. *ACS Omega* **2020**, *5*, 7298–7306. [\[CrossRef\]](#)
24. Hou, X.; Feng, J.; Xu, X.; Zhang, M. Synthesis and Characterizations of Spinel MnFe₂O₄ Nanorod by Seed-Hydrothermal Route. *J. Alloys Compd.* **2010**, *491*, 258–263. [\[CrossRef\]](#)
25. Kafshgari, L.A.; Ghorbani, M.; Azizi, A. Synthesis and Characterization of Manganese Ferrite Nanostructure by Co-Precipitation, Sol-Gel, and Hydrothermal Methods. *Part. Sci. Technol.* **2019**, *37*, 900–906. [\[CrossRef\]](#)

26. Kan, C.C.; Ibe, A.H.; Rivera, K.K.P.; Arazo, R.O.; de Luna, M.D.G. Hexavalent Chromium Removal from Aqueous Solution by Adsorbents Synthesized from Groundwater Treatment Residuals. *Sustain. Environ. Res.* **2017**, *27*, 163–171. [[CrossRef](#)]
27. Ong, D.C.; Pingul-Ong, S.M.B.; Kan, C.C.; de Luna, M.D.G. Removal of Nickel Ions from Aqueous Solutions by Manganese Dioxide Derived from Groundwater Treatment Sludge. *J. Clean. Prod.* **2018**, *190*, 443–451. [[CrossRef](#)]
28. Reddy, D.H.K.; Yun, Y.S. Spinel Ferrite Magnetic Adsorbents: Alternative Future Materials for Water Purification? *Coord. Chem. Rev.* **2016**, *315*, 90–111. [[CrossRef](#)]
29. Xiao, Y.; Liang, H.; Wang, Z. MnFe₂O₄/Chitosan Nanocomposites as a Recyclable Adsorbent for the Removal of Hexavalent Chromium. *Mater. Res. Bull.* **2013**, *48*, 3910–3915. [[CrossRef](#)]
30. Habiba, U.; Joo, T.C.; Siddique, T.A.; Salleh, A.; Ang, B.C.; Afifi, A.M. Effect of Degree of Deacetylation of Chitosan on Adsorption Capacity and Reusability of Chitosan/Polyvinyl Alcohol/TiO₂ Nano Composite. *Int. J. Biol. Macromol.* **2017**, *104*, 1133–1142. [[CrossRef](#)] [[PubMed](#)]
31. Xiao, Y.; Liang, H.; Chen, W.; Wang, Z. Synthesis and Adsorption Behavior of Chitosan-Coated MnFe₂O₄ Nanoparticles for Trace Heavy Metal Ions Removal. *Appl. Surf. Sci.* **2013**, *285*, 498–504. [[CrossRef](#)]
32. Zeiger, E.; Gollapudi, B.; Spencer, P. Genetic Toxicity and Carcinogenicity Studies of Glutaraldehyde—A Review. *Mutat. Res. Rev. Mutat. Res.* **2005**, *589*, 136–151. [[CrossRef](#)]
33. Takigawa, T.; Endo, Y. Effects of Glutaraldehyde Exposure on Human Health. *J. Occup. Health* **2006**, *48*, 75–87. [[CrossRef](#)]
34. Sam, S.; Nesaraj, S. Preparation of MnFe₂O₄ Nanoceramic Particles by Soft Chemical Routes. *Int. J.* **2011**, *9*, 223–239.
35. Sessarego, S.; Rodrigues, S.C.G.; Xiao, Y.; Lu, Q.; Hill, J.M. Phosphonium-Enhanced Chitosan for Cr(VI) Adsorption in Wastewater Treatment. *Carbohydr. Polym.* **2019**, *211*, 249–256. [[CrossRef](#)]
36. Mende, M.; Schwarz, D.; Steinbach, C.; Boldt, R.; Schwarz, S. Simultaneous Adsorption of Heavy Metal Ions and Anions from Aqueous Solutions on Chitosan—Investigated by Spectrophotometry and SEM-EDX Analysis. *Colloids Surf. A Physicochem. Eng. Asp.* **2016**, *510*, 275–282. [[CrossRef](#)]
37. Ahamad, T.; Naushad, M.; Al-Shahrani, T.; Al-hokbany, N.; Alshehri, S.M. Preparation of Chitosan Based Magnetic Nanocomposite for Tetracycline Adsorption: Kinetic and Thermodynamic Studies. *Int. J. Biol. Macromol.* **2020**, *147*, 258–267. [[CrossRef](#)]
38. Wang, G.; Zhao, D.; Ma, Y.; Zhang, Z.; Che, H.; Mu, J.; Zhang, X.; Zhang, Z. Synthesis and Characterization of Polymer-Coated Manganese Ferrite Nanoparticles as Controlled Drug Delivery. *Appl. Surf. Sci.* **2018**, *428*, 258–263. [[CrossRef](#)]
39. Futralan, C.M.; Kan, C.C.; Dalida, M.L.; Hsien, K.J.; Pascua, C.; Wan, M.W. Comparative and Competitive Adsorption of Copper, Lead, and Nickel Using Chitosan Immobilized on Bentonite. *Carbohydr. Polym.* **2011**, *83*, 528–536. [[CrossRef](#)]
40. Giraldo, L.; Erto, A.; Moreno-Piraján, J.C. Magnetite Nanoparticles for Removal of Heavy Metals from Aqueous Solutions: Synthesis and Characterization. *Adsorption* **2013**, *19*, 465–474. [[CrossRef](#)]
41. Lagergren, S.Y. Zur Theorie Der Sogenannten Adsorption Gelöster Stoffe. *K. Sven. Vetensk. Handl.* **1898**, *24*, 1–39. [[CrossRef](#)]
42. Ho, Y.S.; McKay, G. A Comparison of Chemisorption Kinetic Models Applied to Pollutant Removal on Various Sorbents. *Process Saf. Environ. Prot.* **1998**, *76*, 332–340. [[CrossRef](#)]
43. Blanchard, G.; Maunaye, M.; Martin, G. Removal of Heavy Metals from Waters by Means of Natural Zeolites. *Water Res.* **1984**, *18*, 1501–1507. [[CrossRef](#)]
44. Weber, W.J.; Morris, J.C. Kinetics of Adsorption on Carbon from Solution. *J. Sanit. Eng. Div.* **1963**, *89*, 31–59. [[CrossRef](#)]
45. Ren, Y.; Li, N.; Feng, J.; Luan, T.; Wen, Q.; Li, Z.; Zhang, M. Adsorption of Pb(II) and Cu(II) from Aqueous Solution on Magnetic Porous Ferrosin MnFe₂O₄. *J. Colloid Interface Sci.* **2012**, *367*, 415–421. [[CrossRef](#)]
46. Kumar, A.; Yadav, K.L. Synthesis and Characterization of MnFe₂O₄–BiFeO₃ Multiferroic Composites. *Phys. B Condens. Matter* **2011**, *406*, 1763–1766. [[CrossRef](#)]
47. Tran, H.N.; You, S.-J.; Chao, H.-P. Thermodynamic Parameters of Cadmium Adsorption onto Orange Peel Calculated from Various Methods: A Comparison Study. *J. Environ. Chem. Eng.* **2016**, *4*, 2671–2682. [[CrossRef](#)]
48. Tran, H.N.; You, S.-J.; Hosseini-Bandegharaei, A.; Chao, H.-P. Mistakes and Inconsistencies Regarding Adsorption of Contaminants from Aqueous Solutions: A Critical Review. *Water Res.* **2017**, *120*, 88–116. [[CrossRef](#)] [[PubMed](#)]
49. Chella, S.; Kollu, P.; Komarala, E.V.P.R.; Doshi, S.; Saranya, M.; Felix, S.; Ramachandran, R.; Saravanan, P.; Koneru, V.L.; Venugopal, V.; et al. Solvothermal Synthesis of MnFe₂O₄-Graphene Composite-Investigation of Its Adsorption and Antimicrobial Properties. *Appl. Surf. Sci.* **2015**, *327*, 27–36. [[CrossRef](#)]
50. Langmuir, I. The Adsorption of Gases on Plane Surfaces of Glass, Mica and Platinum. *J. Am. Chem. Soc.* **1918**, *40*, 1361–1403. [[CrossRef](#)]
51. Freundlich, H. Über Die Adsorption in Lösungen. *Z. Phys. Chem.* **1906**, *57*, 385–470. [[CrossRef](#)]
52. Temkin, M.J.; Pyzhev, V. Recent Modifications to Langmuir Isotherms. *Acta Physicochim. URSS* **1940**, *12*, 217–222.
53. Dubinin, M.; Radushkevich, L. The Equation of the Characteristic Curve of Activated Charcoal. *Proc. Acad. Sci. USSR* **1947**, *55*, 331–333.
54. Meng, Y.; Chen, D.; Sun, Y.; Jiao, D.; Zeng, D.; Liu, Z. Adsorption of Cu²⁺ Ions Using Chitosan-Modified Magnetic Mn Ferrite Nanoparticles Synthesized by Microwave-Assisted Hydrothermal Method. *Appl. Surf. Sci.* **2015**, *324*, 745–750. [[CrossRef](#)]
55. Sezgin, N. Removal of Copper From Industrial Wastewater Using Manganese Ferrite Nanoparticles: Evaluation Of Equilibrium And Kinetic Model. *Env. Eng. Manag. J.* **2018**, *17*, 2147–2156. [[CrossRef](#)]
56. Wang, Y.; Cheng, R.; Wen, Z.; Zhao, L. Synthesis and Characterization of Single-Crystalline MnFe₂O₄ Ferrite Nanocrystals and Their Possible Application in Water Treatment. *Eur. J. Inorg. Chem.* **2011**, 2942–2947. [[CrossRef](#)]

57. Bateer, B.; Tian, C.; Qu, Y.; Du, S.; Yang, Y.; Ren, Z.; Pan, K.; Fu, H. Synthesis, Size and Magnetic Properties of Controllable MnFe_2O_4 Nanoparticles with Versatile Surface Functionalities. *Dalton Trans.* **2014**, *43*, 9885–9891. [[CrossRef](#)]
58. Jung, K.-W.; Lee, S.Y.; Lee, Y.J. Facile One-Pot Hydrothermal Synthesis of Cubic Spinel-Type Manganese Ferrite/Biochar Composites for Environmental Remediation of Heavy Metals from Aqueous Solutions. *Bioresour. Technol.* **2018**, *261*, 1–9. [[CrossRef](#)]
59. Israelachvili, J.N. Interactions Involving Polar Molecules. In *Intermolecular and Surface Forces*; Elsevier: Amsterdam, The Netherlands, 2011; pp. 71–90.
60. Kara, İ.; Yilmazer, D.; Akar, S.T. Metakaolin Based Geopolymer as an Effective Adsorbent for Adsorption of Zinc(II) and Nickel(II) Ions from Aqueous Solutions. *Appl. Clay Sci.* **2017**, *139*, 54–63. [[CrossRef](#)]
61. Kumar, S.; Nair, R.R.; Pillai, P.B.; Gupta, S.N.; Iyengar, M.A.R.; Sood, A.K. Graphene Oxide– MnFe_2O_4 Magnetic Nanohybrids for Efficient Removal of Lead and Arsenic from Water. *Acs Appl. Mater. Interfaces* **2014**, *6*, 17426–17436. [[CrossRef](#)]
62. Shirkhodaie, M.; Beyki, M.H.; Shemirani, F. Simple Route Synthesis of MnFe_2O_4 @ Alunite Composite for Preconcentration of Trace Level of Copper and Lead from Food and Water Samples. *Desalination Water Treat.* **2016**, *57*, 22480–22492. [[CrossRef](#)]